JGR Planets

RESEARCH ARTICLE

10.1029/2026JE009704

Influence of Mars Topography on Radiation Dose Detected by the Mars Science Laboratory and Assessment of Mars Surface Albedo Radiation

Jingnan Guo[1], Changqi Tian[1], Gabin Charpentier[2,3], Robert F. Wimmer-Schweingruber[4], Salman Khaksarighiri[4], Lu Pan[1], Jan Leo Löwe[4], Bent Ehresmann[5], Donald M. Hassler[5], Cary Zeitlin[6], Daniel Matthiä[7], Thomas Berger[7], and Günther Reitz[7]

[1]National Key Laboratory of Deep Space Exploration/School of Earth and Space Sciences, University of Science and Technology of China, Hefei, China, [2]Centre National D'Études Spatiales (CNES), Toulouse, France, [3]TRAD Tests & Radiations, Labège, France, [4]Institute of Experimental and Applied Physics, Christian-Albrechts-University, Kiel, Germany, [5]Solar System Science & Exploration Division, Southwest Research Institute, Boulder, CO, USA, [6]Leidos Corporation, Houston, TX, USA, [7]German Aerospace Center (DLR), Institute of Aerospace Medicine, Cologne, Germany

Key Points:

- The influence of varying terrain topographies on the dose rate measured by Curiosity traversing through Gale crater is studied
- Dose contributed by particles from different sky directions and by those from the terrain is determined combining modeling and measurements
- The surface upward radiation dose (on flat terrain) is between ~18%–24% of the total dose

Correspondence to:

J. Guo, C. Tian and G. Charpentier,
jnguo@ustc.edu.cn;
tchangqi@mail.ustc.edu.cn;
gabincharpentier@gmail.com

Citation:

Guo, J., Tian, C., Charpentier, G., Wimmer-Schweingruber, R. F., Khaksarighiri, S., Pan, L., et al. (2026). Influence of Mars topography on radiation dose detected by the Mars Science Laboratory and assessment of Mars surface albedo radiation. *Journal of Geophysical Research: Planets*, *131*, e2026JE009704. https://doi.org/10.1029/2026JE009704

Received 29 JAN 2026
Accepted 1 APR 2026

Abstract The Radiation Assessment Detector (RAD) on the Curiosity rover has been characterizing the Martian surface radiation field since 2012. The dose observed by RAD is influenced by a variety of factors, including an essential one, the terrain. After parking near Murray Buttes in September 2016 where it first detected a ~5% decrease in dose rate, the rover has passed a series of other interesting terrains where we find decreases in the dose rate reaching 19%. This radiation reduction is due to extra shielding provided by the nearby surface structure, confirming the potential use of surface structures for radiation protection of humans on Mars. Combining a zenith-angle-dependent radiation model and the rover panoramic visibility map we calculate the downward radiation dose that RAD should observe under different topographic shielding conditions. This allows us to further evaluate the terrain-generated albedo dose at different locations. We finally estimate that on a flat surface the albedo radiation is between ~18% and 24% of the total surface dose. This study contributes to developing a realistic terrain-based radiation map which is important for future Mars explorers.

Plain Language Summary Mars lacks a global magnetic field and its atmosphere is very thin compared to that of Earth. Thus its surface is exposed to energetic particles from space which may pose risks to future humans on Mars. Local topography, such as valleys, hills, and varied landscapes, can block or modify some of the radiation coming from the sky and provide some reduction in radiation dose. Since landing on Mars in 2012, the Radiation Assessment Detector (RAD) on NASA's Curiosity rover has observed some decreases of the radiation dose rate while Curiosity passed by topographic structures including buttes, hills etc., which are studied in detail here. Moreover, combining RAD observations with a radiation transport model, we estimate the contribution of secondary radiation generated in the soil of Mars and emitted outward (upward) from the surface to be approximately 18%–24% of the total surface dose. Our study contributes to mapping the realistic radiation field considering the surface topography of Mars, which is important for future Mars explorers.

1. Introduction

Lacking a global magnetosphere and a thick atmosphere, the Martian surface is directly exposed to space radiation, which may affect the health of astronauts landing on Mars in the future (Cucinotta et al., 2017; Walsh et al., 2019). Space radiation reaching Mars consists mainly of the background Galactic Cosmic Ray (GCR) particles and Solar Energetic Particles (SEPs). The primary space radiation can either directly propagate through the atmosphere or generate secondary particles therein. When reaching the surface, they can also generate secondary particles in the terrain that may escape back to the surface as albedo particles.

To evaluate such radiation risks and also to provide the needed radiation data as input to radiation risk models, the Radiation Assessment Detector (RAD, Hassler et al., 2012; Zeitlin et al., 2016; Figure 1) was designed to measure the energetic particle environment on the Martian surface as part of the Mars Science Laboratory (MSL) mission (Grotzinger et al., 2012), which landed the Curiosity rover in Gale Crater in August 2012. The RAD sensor head contains several detectors for energetic particle measurements: three silicon detectors (A, B, and C), a CsI scintillator (D), a plastic scintillator (E), and an additional plastic scintillator (F) that surrounds D and E and acts

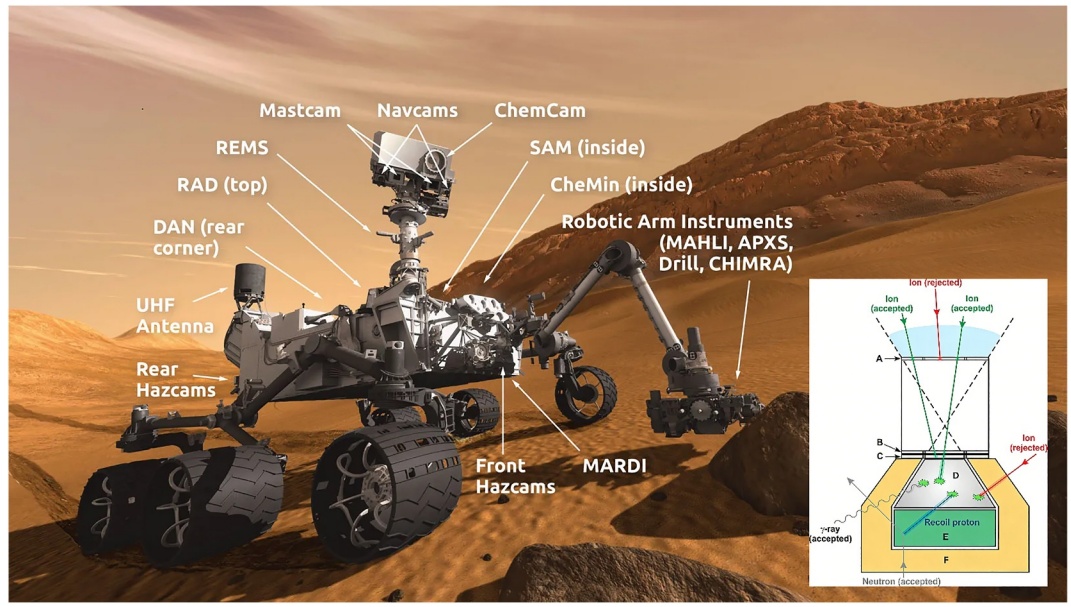

Figure 1. Instruments on the Curiosity rover (image credit: NASA/JPL-Caltech, more details can be found here: https://science.nasa.gov/mission/msl-curiosity/science-instruments/) and schematic diagram of RAD (bottom right corner, taken from Hassler et al. (2012)).

as anticoincidence for neutral particle detection. The telescope detector configuration (from A to E) measures incoming (mainly downward) charged particles and their Linear-Energy-Transfer (LET) spectra within a zenith angle of about 36°. The absorbed dose rate is concurrently measured in two active dosimeters, silicon detector B and plastic scintillator E. The latter has much better statistics due to a large geometric factor. It has a density similar to that of human tissue and is more sensitive to neutrons than the silicon detector B. Besides, low-energy albedo particles traveling upward from the surface are likely to deposit energy in detector E but may stop in the detector stack (or scatter out of the stack) before reaching detector B. Therefore, we adopted the absorbed dose in the plastic detector E here to study the albedo radiation.

The varying natural topography on the Martian surface, that is hills, crevasses, passes, craters, etc., can influence radiation levels by blocking part of the sky and also by contributing additional albedo particles. The first observational confirmation of this topographic effect was provided by Ehresmann et al. (2021) and Guo et al. (2021), which used RAD measurements near Murray Buttes (in September 2016) where RAD detected a decrease of 4%–5% in dose rate when the blocked sky ratio was approximately 19%. Combining a zenith-angle-dependent radiation model (Khaksarighiri et al., 2023) and the panoramic visibility map of the rover, Guo et al. (2021) then derived a ∼12% reduction in the dose from downward directed particles due to obstruction, higher than the observed decrease of 5%. The authors attributed this difference to the additional albedo radiation from the butte and further estimated the flat-surface albedo dose to be approximately 19% of the total surface dose. Additionally, the Dynamic Albedo of Neutrons (DAN, Litvak et al., 2008) instrument on the Curiosity rover measures neutrons that have undergone interactions with rocks and materials in the rover's local environment. DAN has observed that increased thermal neutron count rates may be correlated with increased average local relief (Dibb et al., 2024), supporting the idea that increases in surface shielding would increase albedo particles.

This work follows the same methodology as in Guo et al. (2021) but employs 5 new sites of interest encountered by MSL since 2020, including Tower Buttes in February 2020, Bloodstone Hill in June 2020, Mount Mercou in March 2021, Maria Gordon Notch in December 2021, and Paraitepuy in August 2022. Specifically, the topographic shielding as a function of the zenith angle and also the azimuthal angle for each location is obtained by 3D reconstruction of the surface geometry from the point of view of the rover using a DEM (Digital Elevation Model) created by JPL/NASA/USGS/University of Arizona (https://astrogeology.usgs.gov/search/map/mars_msl_gale_merged_dem_1m) (Charpentier et al., 2026). Combining a zenith-angle-dependent Mars radiation model and the above topographic information, the reduction of the dose from the sky direction is estimated, and meanwhile the increase of albedo contribution due to extra shielding is derived for each location. Finally, flat-terrain albedo

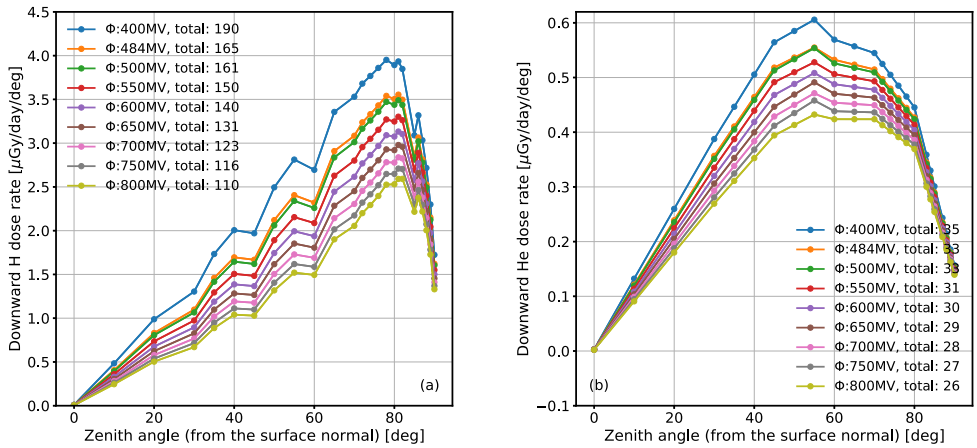

Figure 2. Modeled results of the dependence of RAD E dose rate on zenith angle, θ, for (a) GCR protons and (b) helium ions arriving at Mars. Different primary GCR spectra are considered under different solar modulation potential, ϕ, as inputs to the BON model, as explained in Section 2. The full-sky dose rates (μGy/d) integrated over θ are also given in each case. Figure taken from Guo et al. (2021).

radiation is assessed to be between ∼18% and 24% of the total surface dose, a result consistent with the previous assessment of 19% based on Murray Buttes alone (Guo et al., 2021). This study contributes to developing a realistic terrain-based radiation exposure map which is important for future Mars explorers.

The paper is organized as follows. Section 2 will describe the zenith-angle-dependent Mars surface radiation transport model and the GCR flux input of the model. Section 3 will show the observational results of how dose rate varies at different terrain. Section 4 will combine the observation and model to derive the surface downward and albedo dose at each of selected sites. Section 5 will summarize and discuss about the results.

2. Modeling the Surface Downward Dose

The Martian surface radiation environment can be studied via particle transport modeling through the Martian atmosphere and surface (Charpentier et al., 2024; De Angelis et al., 2006; Gronoff et al., 2015; Guo et al., 2019; Keating et al., 2005; Kim et al., 2014; Saganti et al., 2004; Zhang et al., 2022, etc.). The successful operation of RAD on Mars also made it possible to benchmark these models against in situ measurements (e.g., Guo et al., 2019; Khaksari et al., 2025; Matthiä et al., 2016, 2017). The model used in this work has the particular feature that the zenith-angle dependence of the downward-directed dose is provided as shown in Figure 2 (see more explanation later). Although dose as a physical quantity should not have directionality, in this article we use the simplified term "downward dose" to refer to the dose from downward directed particles.

The input primary GCRs of the Mars radiation model can be obtained by physics-based or empirical GCR models (see a recent review and comparison of different models by Liu et al. (2024)). Our study adopts the Badhwar-O'Neill (BON) 2014 GCR model which gives the GCR spectrum at 1 AU via transport modeling of GCRs from the local interstellar spectrum (O'Neill et al., 2015). The strength of the modulation is quantified by the so-called "modulation potential" ϕ in the BON model which is normally determined monthly for Earth. Thus, ϕ represents the heliospheric modulation of GCRs that follows the long-term solar cycle evolution (e.g., Potgieter, 2013; Usoskin et al., 2011). Consequently, the predicted GCR flux of the model is anti-correlated with ϕ. We will briefly introduce the Mars surface downward-dose model in Section 2.1 and show the procedure to derive the input parameter ϕ at Mars for the selected time of interest in Section 2.2.

2.1. The Zenith-Angle Dependence Model

The directionality of the incoming particles is not registered in the RAD dose-rate data, which would have provided essential information for understanding the topographic shielding effects. Exploiting the rover tilting information, Wimmer-Schweingruber et al. (2015) have studied the dependence of the surface particle fluxes on

zenith angle (θ, the angle from the surface normal) and found that within a narrow range of rover tilt angles ($\leq 15°$), the radiation field is nearly, but not entirely isotropic, that is, the flux is determined to be $\propto \cos^{\gamma}(\theta)$ with $\gamma = 1.18 \pm 0.07$ (In an isotropic field, γ is exactly 1). In order to quantify the directionality of the dose on the surface of Mars over a wide range of θ, we employ a model that uses the Monte Carlo GEANT4 approach (Agostinelli et al., 2003; Allison et al., 2006, 2016) to track the GCRs that propagate through the Martian atmosphere and reach the surface of Mars from different zenith angles so that the result provides the angular dependence of the downward-directed surface dose (Guo et al., 2021; Khaksari et al., 2025; Khaksarighiri et al., 2023).

Since the Martian atmosphere is composed of 95% of CO_2, the model approximates the Martian atmosphere as a spherical shell of CO_2 gas surrounding the RAD instrument phantom. The vertical atmospheric mass (zenith angle $\theta = 0°$) is set as 21 g/cm^2, which approximately corresponds to an average surface pressure of about 800 Pa as measured by MSL's Rover Environmental Monitoring Station (REMS, Gómez-Elvira et al., 2012). The thickness of the atmosphere increases with θ to account for a realistic 3D atmospheric structure. The sky hemisphere is segmented into multiple θ-dependent rings where particles were launched with an inward cosine directional distribution towards the Martian surface. The final dose for each θ-angle recorded in the model comprises all primary particles and secondary particles generated by these primaries interacting with the atmosphere which are detected by the RAD. Only GCR protons and helium ions are modeled as they make up about 99% of the GCR atomic nuclei. Heavier ion Monte Carlo calculations are computationally very expensive and thus ignored in the original model, but their contributions to the surface dose will be additionally considered as shown later in Section 4. All downward doses of primary and secondary particles arriving at the surface that reach the phantom RAD B and E detectors have been counted in the model. More detailed description and verification of the model can be found in Khaksarighiri et al. (2023) and Khaksari et al. (2025).

Figure 2 presents the modeled zenith-angle dependence of the dose rate in the RAD E detector under different solar modulation potentials ϕ with $d_{\mathrm{GCR_H}}(\theta)$ for primary GCR protons in the left panel and $d_{\mathrm{GCR_{He}}}(\theta)$ for helium ions in the right panel. The modeled results show that the radiation dose on Mars is dependent on θ which corresponds to different atmospheric depth. For instance, the atmospheric column depth increases from about 21 g/cm^2 at $\theta = 0°$ to more than 300 g/cm^2 at angles above 85° (Khaksarighiri et al., 2023). A longer path will substantially slow down primary particles that become more ionizing or more easily stopped; meanwhile, the probability of the initial ion getting scattered away from the original beam, undergoing a nuclear interaction and fragmenting into lighter ions (in case of a heavy GCR ion) is greater with a longer path.

Figure 2 shows that protons arriving at $\theta \sim 80°$ make the greatest contribution to the surface dose per degree of zenith angle while for helium ions this peak is around 55°. The results are balanced by two factors: (a) particles need to transport through larger depths to reach the surface at a larger zenith angle θ, and (b) the solid angle for each degree of θ subtended at larger zenith angles is greater than that at smaller angles. Ions with more mass fragment more easily in the atmosphere, so helium ions penetrate shorter distances than protons in the atmosphere. Considering that atmospheric depth increases with the zenith angle θ, the peak-dose zenith angle for helium ions is smaller than that for protons. We also note some non-smooth features (e.g., at 45, 60 and 85° for protons) that are due to a combination of uncertainties in the transport models and statistical variations. However, these features do not affect the integration results as we smoothed the functions and found that the integrated doses are the same as those from original non-smoothed functions within a difference of 1 μGy/d.

2.2. The Modulation Potential ϕ at Mars

As shown in Figure 2, the surface dose rate depends on solar modulation, with a smaller ϕ (weaker modulation) resulting in a larger dose rate for each θ. The dose rate summed over θ from 0 to 90° represents the total downward-directed dose rate on the surface under a certain ϕ value. The dose induced by all primary GCR protons is 4.2–5.4 times (depending on ϕ) higher than that induced by all primary GCR helium ions (see legends in Figure 2).

For studying the long-term modulation effect over months and years, the longitudinal difference of modulation between Mars and Earth can be ignored and previous studies have approximated ϕ at Mars to be the same as that at Earth (Guo et al., 2015). However, for the time scale of days which is the case here, the modulation condition can

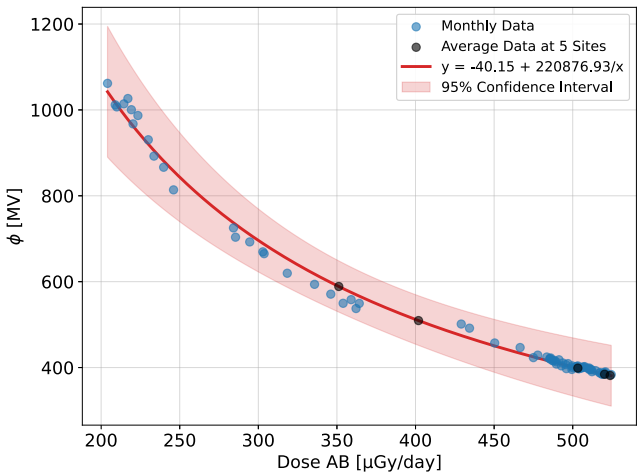

Figure 3. The correlation between monthly ϕ tabulated by the BON 2014 model and dose measured by TGO Liulin-MO AB detector pair at Mars's orbit from May 2018 to July 2024. The black dots show the ϕ averaged for each of the 5 periods studied here. The fitting function and 95% confidence interval and prediction interval are also shown.

be significantly different at the two planets when they are impacted by solar transients (e.g., Freiherr von Forstner et al., 2020; Lee et al., 2017).

In order to better assess the heliospheric modulation at Mars, we use the radiation data provided by the Liulin-MO radiation detector on the ExoMars Trace Gas Orbiter (TGO) at Mars as a reference, since it is not affected by the topographical changes on the surface as experienced by MSL/RAD. In May 2018, TGO was inserted to its Mars Science Orbit (MSO) with a circular orbit of 400 km altitude, indicating that shading of deep space isotropic radiation by Mars stays mostly constant over time. The orbital period is around 2 hr, while we adopt daily or monthly averaged values (as shown later) so that the slight orbital effect, for example, the weak influence by Mars magnetosphere, is also minimized. TGO/Liulin-MO contains two dosimetric telescopes-A&B, and C&D arranged at two perpendicular directions (Semkova et al., 2018). Each pair of the dosimetric telescopes consists of two 300 μm thick, 20 × 10 mm area rectangular Si PIN photodiodes and provides data in the energy deposition range 0.08–190 MeV. Theoretically, the dose rates provided by these two pairs of detectors should be the same. However, dose AB has a smaller statistical variance as it bears less noise contamination (Liu et al., 2023), we use dose AB in this study.

To derive the daily ϕ at Mars based on TGO measurements, we need to first obtain the empirical function between ϕ and TGO dose rate. Considering the 27-day rotation of the Sun, monthly ϕ at Mars's longitude is approximately the same as that at Earth. Thus, the monthly average value of TGO AB dose rate, D_{TGO} is correlated with the monthly ϕ of the BON model from May 2018 to July 2024 which covers all the dates of scenarios studied here. The function below can be used to fit D_{TGO} and ϕ values following Guo et al. (2015):

$$\phi_{\mathrm{Mars}} = a + \frac{b}{D_{\mathrm{TGO}}} \quad (1)$$

The fitted parameters are $a = -40.15 \pm 5.33$ MV and $b = 220876.93 \pm 1{,}936.56$ MV · μGy/d. Figure 3 shows the nice correlation ($R^2 = 0.99$) and the fitted function of the two quantities. Substituting the daily value of TGO Liulin-MO/AB dose rate into Equation 1, the daily modulation potential can be obtained as ϕ_{Mars} at Mars's longitude, but at a distance of 1 AU.

As known, GCRs are transported from outside the solar system towards the inner-heliosphere, thus there is also a slight radial gradient of GCR flux. According to multi-spacecraft observations, this gradient is only about 2%–4% per AU between 1 AU and 5 AU (Honig et al., 2019; Roussos et al., 2020). Since the BON model predicts the GCR flux at 1 AU, we also adopt a flux enhancement of 1.5% based on the BON spectra to derive the actual flux at Mars (1.5 AU).

In summary, we adopt the BON GCR proton and helium ion spectra as input of our Mars radiation transport model with two adjustments in comparison to the work by Guo et al. (2021). First, we consider daily ϕ_{Mars} derived from TGO measurements at Mars to obtain the spectra of the BON model. Second, we scale the flux by 1.015 to account for the GCR radial gradient. The Mars radiation transport model will then provide the zenith-angle dependent dose rate for any day/location of interest as shown in the next section.

3. The Influence of Terrain on Radiation Dose

After it had parked at Murray Buttes in September 2016, Curiosity passed by a few more sites with interesting topography, including Tower Buttes, Bloodstone Hill, Mt Mercou, Maria Gordon Notch and Paraitepuy between 2020 and 2022. Figure 4 shows the RAD E dose rate together with the derived daily ϕ_{Mars} at Mars's longitude when the rover passed these five sites. The eight periods highlighted in red represent eight parking windows during which a notable reduction in the dose rate can be observed in each case and are named "P1" to "P8." The transparent gray areas mark the background condition before or after each parking and are named "BG1" to "BG8." Note that "P4" and "P5" share the same background marked "BG4/5."

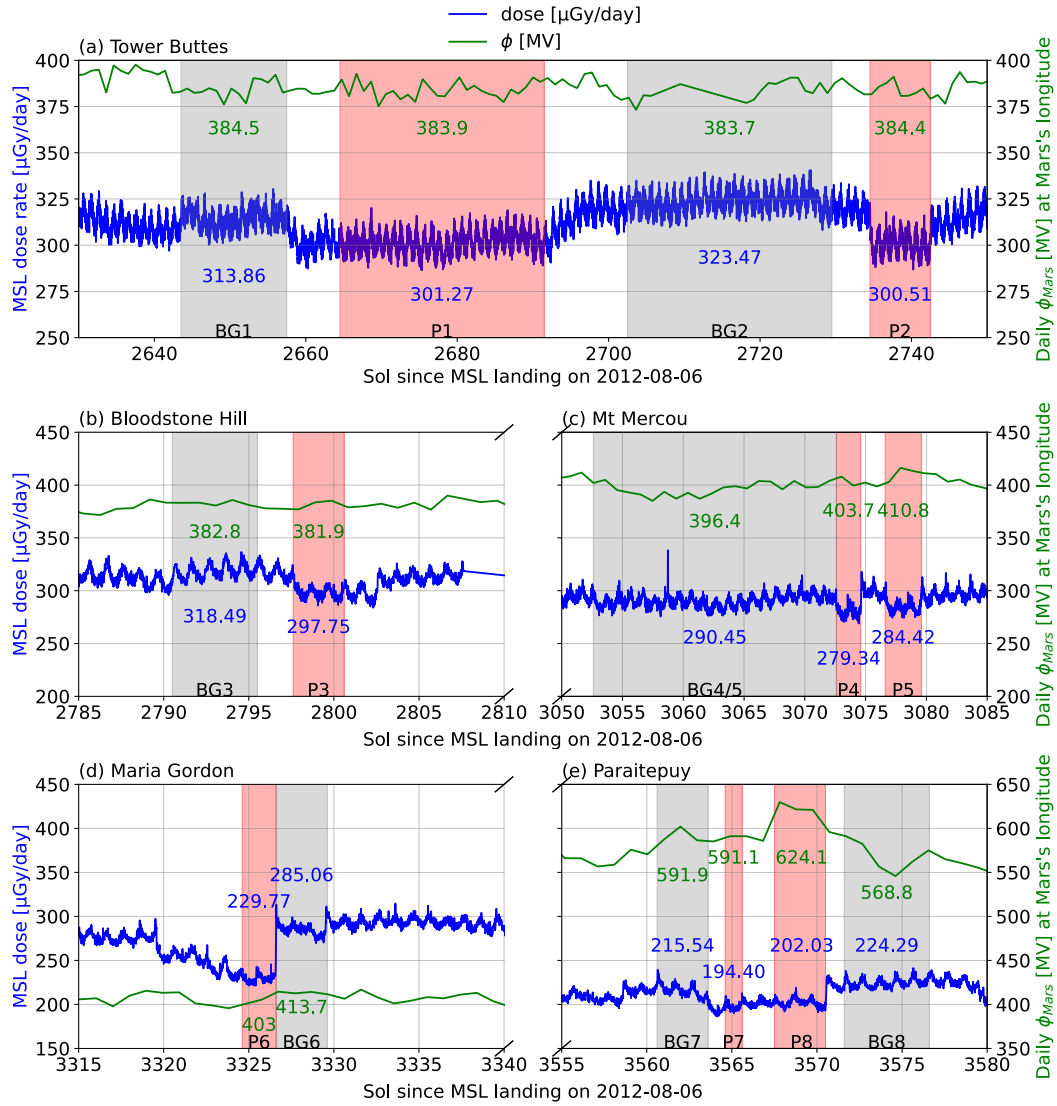

Figure 4. The derived daily ϕ (green, right y-axes) for Mars based on TGO observations (ϕ is a parameter that modulates the input GCR flux at Mars as detailed in Section 2.2) and the RAD E dose rate (blue, left y-axes) when the rover passed different terrain features as detailed in Section 3. The red highlighted areas represent the eight periods when the rover was parked near enhanced-shielding structures and are named "P1" to "P8." The gray shaded areas represent the background periods when the rover was relatively far away from the specific shielding structures and are named "BG1" to "BG8." The average ϕ and dose rate of each marked period are shown as texts.

The numbers indicated in blue beneath the dose rate curve give the values of dose rate averaged over each background or parking period. Comparing the background and parking dose rate values, we found a decrease of about 4%–7% for Tower Buttes (Figure 4a), ∼7% for Bloodstone Hill (Figure 4b), 2%–4% for Mt Mercou (Figure 4c), 19% for Maria Gordon Notch (Figure 4d) and ∼10% for Paraitepuy (Figure 4e). Note that the dose rate also changes at a daily frequency due to diurnal atmospheric variations caused by the enhanced daily thermal tide at Gale Crater (Rafkin et al., 2014). Since we always consider the mean dose rate averaged over a few days, this daily effect does not affect our analysis. The aforementioned dose rate and the observed decrease in dose rate during each parking are given in Table 1.

The numbers marked near ϕ values in green give the values of ϕ averaged over each background or parking period. As shown, the modulation conditions at Mars did not vary significantly between the background and parking periods in each scenario. However, some small oscillations are still present in the ϕ data, thus the input ϕ of the BON GCR model is adjusted for each period, as also shown in Table 1.

Table 1
For Each Selected Location and Period, We Show, From Left to Right, the Observed Dose Rate in RAD E Detector D_{RAD}, the Percentage of Dose Rate Decrease Comparing the Parking and the Background Period, Average ϕ Derived for Mars, Together With Modeled Surface-Downward Dose Contributed by Primary GCR Protons D_{GCR_H}, Helium Ions $D_{GCR_{He}}$, and Total Sky Dose D_{sky} (With Additional Heavier Ion Contributions), the Model-Predicted Decrease of Downward Dose During the Parking, As Well As the Ratio of Obstructed Sky to the Full Sky, Derived Albedo Dose on a Flat Terrain (FT) and Its Proportion to the Measured Total Dose D_{RAD}

Location	Period	D_{RAD}[μGy/d]	Measured decrease	ϕ[MV]	D_{GCR_H}[μGy/d]	$D_{GCR_{He}}$[μGy/d]	D_{sky}μGy/d]	D_{sky}decrease	$\sum ROS(\theta)\cdot\delta_\theta$	FT D_{albedo}[μGy/d]	FT Albedo proportion
Tower Buttes	BG1	313.9	–	384.5	181.7	35.0	238.3	–	7.9%	70.0	21.5
	P1	301.3	4.0%	383.9	169.0	33.6	222.8	6.5%	13.7%	69.0	21.3
	BG2	323.5	–	383.7	186.5	35.5	244.2	–	5.4%	75.2	22.7
	P2	300.5	7.1%	384.4	165.9	33.2	219.0	10.3%	14.8%	71.0	21.7
Bloodstone Hill	BG3	318.5	–	382.8	183.2	35.1	240.1	–	7.2%	73.1	22.2
	P3	297.8	6.5%	381.9	170.5	33.5	224.5	6.5%	12.7%	65.0	20.2
Mt Mercou	BG4/5	290.5	–	396.4	167.0	33.5	222.7	–	11.8%	60.6	19.4
	P4	279.3	3.8%	403.7	161.5	32.5	213.3	4.2%	14.4%	57.7	18.8
	P5	284.4	2.1%	410.8	165.9	33.1	218.9	1.7%	11.4%	58.8	19.3
Maria Gordon Notch	BG6	285.1	–	413.7	152.4	31.6	202.5	–	18.0%	70.0	22.2
	P6	229.8	19.4%	403	114.9	24.8	153.7	24.1%	37.9%	55.2	18.1
Paraitepuy	BG7	215.5	–	591.9	106.7	26.2	146.2	–	22.1%	56.8	22.9
	P7	190.4	9.8%	591.1	90.2	23.3	124.9	14.6%	32.8%	52.4	21.5
	BG8	224.3	–	568.8	118.8	28.2	161.7	–	17.8%	53.1	21.3
	P8	202.0	9.9%	624.1	91.0	23.7	126.0	22.0%	29.6%	58.6	24.2

The paths of the rover traversing the five sites are shown in Figures 5a–9a which are cropped from maps provided by NASA at https://science.nasa.gov/mission/msl-curiosity/location-map/). Each drive is connected with lines in these maps. Drives/Locations corresponding to BG1-8 and P1-8 are also marked. Figures 5b–9b show the relative distance from the landing site with landing-x in the north–south direction, landing-y in the east–west direction. The elevation gives the height of the Curiosity rover in the MOLA (Mars Orbiter Laser Altimeter) coordinate. Figures 5c, 5e, 6c, 7c, 8c, and 9c and 9e show the panoramic sky visibility of the rover as a function of the azimuth angle from 0 to 360° (0° for the North) where the obstructed zenith angle (OZA) for each of the BG1-8 and P1-8 periods is shown. These fields of view were computed using a Digital Elevation Model (DEM) of Gale crater from JPL/NASA/USGS/University of Arizona (https://astrogeology.usgs.gov/search/map/mars_msl_gale_merged_dem_1m), with a spatial resolution of 1 m/pixel (Charpentier et al., 2026). The viewpoint was set 1 m above the surface to mimic the height of MSL/RAD onboard the Curiosity rover. The elevation angle of the horizon was determined for all azimuth angles from 0 to 360°, with bins of 0.25°, within a radius of 20 km around the observation point. After integrating the obstructed azimuthal angle for each zenith angle, we can obtain the ratio of the obstructed sky (ROS) with respect to a full-sky view as a function of the zenith angle θ as shown in Figures 5d, 5f, 6d, 7d, 8d, and 9d and 9f for each selected background and parking period. We should note that due to the complex topography through which the rover was driving, the "background" periods BG1-8 do not have a full-sky view either, but they are usually less shadowed than the "interesting" parking periods P1-8. In the next five subsections (Sections 3.1–3.5), we will describe the main features of the rover traveling through each site, respectively.

3.1. Tower Buttes

Figures 5a and 5b show the path of the rover through Tower Buttes. Between sol 2643.5 and 2657.5 (BG1), the rover was in a valley between the hills and the modulation condition was also stable, consequently the detected dose rate is at a relatively stable level and thus selected to be the background "BG1." After that, the rover headed south and parked near a butte for about 27 sols between sol 2664.5–2691.5 (P1) during which we find an obvious dose rate drop of 4% (Figure 4a). Next, the rover headed further south and drove to a slightly

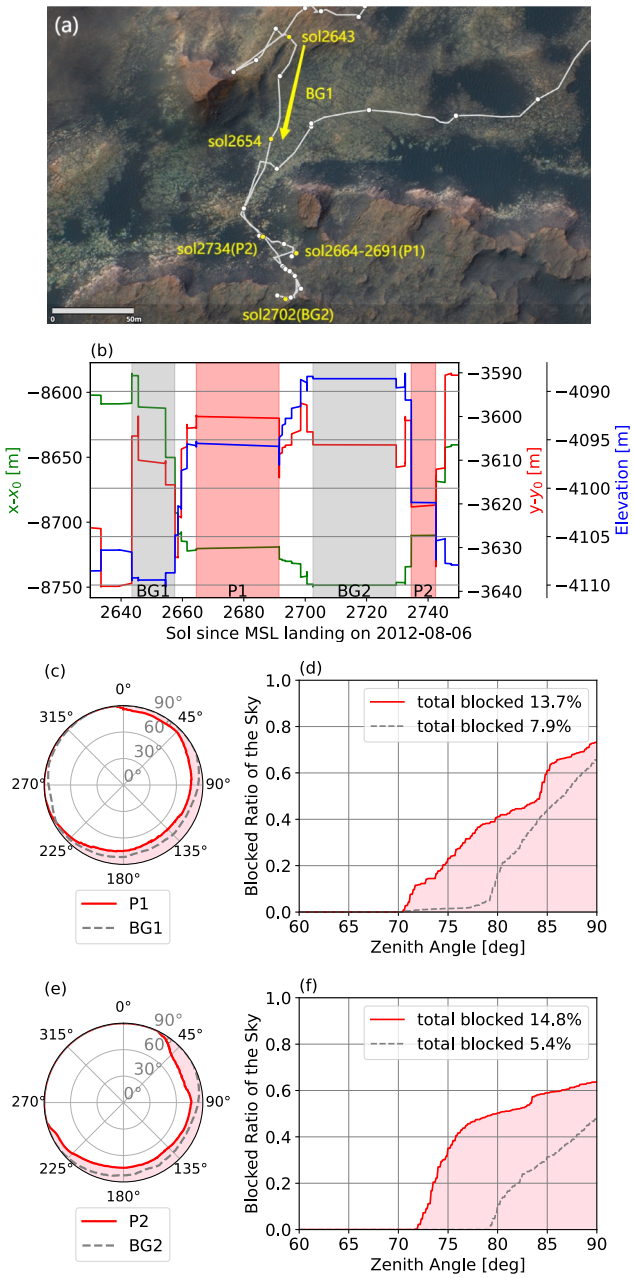

Figure 5. (a) The rover traverse map through the Tower Buttes area (cropped from figures provided by NASA at https://science.nasa.gov/mission/msl-curiosity/location-map/). North is up. Each drive is marked as dots with the ones related to BG1-2 and P1-2 in red. Panel (b) the *x*–*y* coordinates (*x* points to North, *y* points to East) of the rover with respect to the landing site (x_0, y_0) and the elevation in MOLA coordinates. The *x* and *y* coordinates are shown in green and red while the elevation is shown in blue. The parking and background periods are also highlighted using the same time periods introduced in Figure 3. Panel (c) the panoramic sky visibility of RAD as a function of the 360° azimuth angle (0° for North). The zenith angle of obstructed view during P1 is shaded in red whereas that during BG1 is outlined by a gray dashed line. Panel (d) the ratio of blocked sky view with respect to a full sky view as a function of zenith angle for the two periods (P1 and BG1). Panels (e)/(f): same as Panels (c)/(d), but for P2 and BG2.

elevated place where it parked between sol 2702 and 2729 (BG2) and returned northward thereafter. Between sol 2734.5 and sol 2742.5 (P2), the rover parked near another butte where we observed another obvious drop in the dose rate of 7%.

Figure 5c shows the panoramic sky visibility for RAD as a function of the 360° azimuth angle. The OZA during P1 is shown in a transparent red area outlined by a red solid curve, while that during BG1 is shown in a gray-dashed curve. During P1, the OZA ranges from 90° corresponding to the horizon up to about 70° (most shielded in the southeast direction). Instead, OZA of BG1 averaged over four drives during this period is between 90° and 78°. Figure 5d shows the ROS as a function of the zenith angle θ for P1 and BG1. The values integrated over θ are 13.7% and 7.9% for P1 and BG1, respectively, as also shown in Table 1.

Similarly, Figure 5e shows the zenith angle of the obstructed sky as a function of the azimuth angle during P2 and BG2. During P2, the OZA range is down to about 72° (most shielded in the southeast direction), while the OZA range is smaller averaged over BG2: down to about 80°. Figure 5f shows the ROS as a function of the zenith angle θ for P2 and BG2. The values integrated over θ are 14.8% and 5.4% for P2 and BG2, respectively, as also recorded in Table 1.

3.2. Bloodstone Hill

The path of the rover traversing the area of Bloodstone Hill is shown in Figures 6a and 6b. Between sol 2790.5 and sol 2795.5 (BG3), the rover's elevation did not change much, the solar modulation was almost constant, and the dose rate was at a relatively stable level (Figure 4). Then the rover headed southeast and parked near a boulder between sol 2797.6 and sol 2800.6 (P3) during which we find a dose rate decrease of 6.5% (Figure 4b).

Figure 6c shows the panoramic sky visibility of the rover during P3 and BG3. The OZA is between 90° and 77° averaged for BG3, while during P3, the OZA ranges from 90° to about 66° (most shielded in the southeast direction). Figure 6d shows the ROS as a function of the zenith angle for P3 and BG3. The ROS values integrated over θ are 12.7% and 7.2% for P3 and BG3, respectively (also listed in Table 1).

3.3. Mt Mercou

The path of the rover traversing the Mt Mercou area is shown in Figures 7a and 7b. Between sol 3052.6 and sol 3072.6 (BG4/5), the rover parked for 20 sols not far from a boulder. After that, the rover headed south and parked near the boulder between sol 3072.6 and sol 3074.6 (P4), during which we find a dose decrease of 3.8% (Figure 4c and Table 1). Then the rover headed west and parked between sol 3076.6 and sol 3079.6 (P5) during which we find a dose rate drop of 2.1%, compared to that during BG4/5 (Table 1).

Figure 7c shows the OZA as a function of azimuthal angle during P4, P5 and BG4/5. During P4 and P5, the OZA ranges from 90° towards the horizon to about 60° and 67° (most shielded near the southern direction), respectively. During BG4/5, the OZA is between 90° to about 67°. Figure 7d shows the ROS for P4, P5 and BG4/5, which are integrated to be 14.4%, 11.4% and 11.8%, respectively (also shown in Table 1).

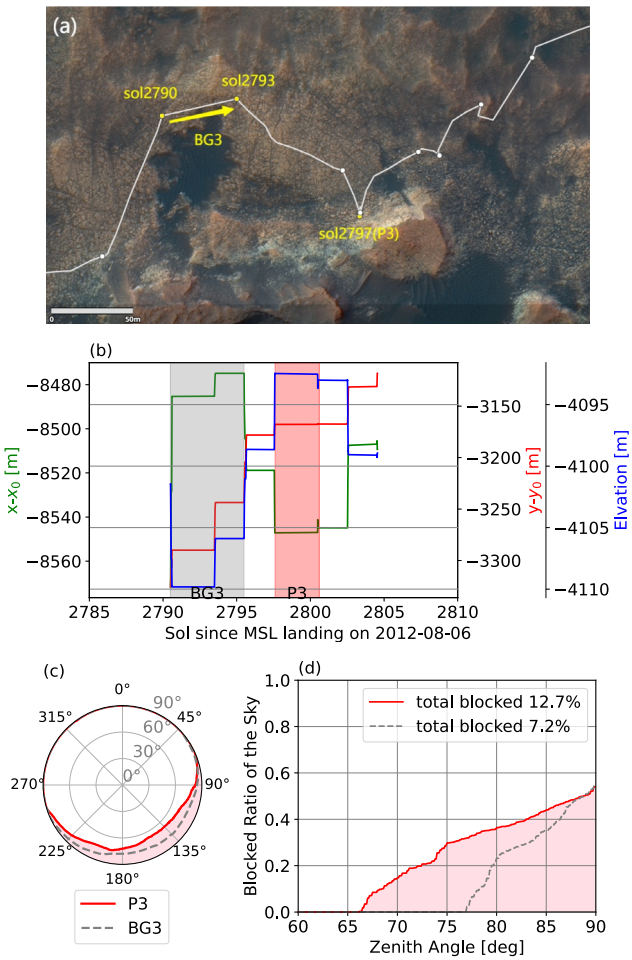

Figure 6. Similar to Figure 5, but for the Bloodstone Hill area.

3.4. Maria Gordon Notch

The path of the rover traversing the Maria Gordon Notch area is shown in Figures 8a and 8b. Between sol 3324.6 and sol 3326.6 (P6), the rover parked in a very narrow valley near a cliff. On sol 3326.6, it drove away and parked relatively far from the previous cliff until sol 3329.6 (BG6). Compared to BG6, we find a dose rate drop of 19% in P6 (Figure 4d).

Figure 8c shows the zenith angle of obstructed view during P6 and BG6. During P6, the OZA ranges from 90° towards the horizon to about 42° (most shielded in the west direction). This reaches the smallest OZA among all the sites selected in this study. During BG6, the shielding is relatively smaller, but the OZA still ranges between 90° and about 61° as the valley is quite narrow. Figure 8d shows the ROS as a function of θ for P6 and BG6, which are integrated to be 37.9%, 18%, respectively (also shown in Table 1).

3.5. Paraitepuy

The path of the rover traversing the Paraitepuy area is shown in Figures 9a and 9b. Between sol 3560.6 and sol 3563.6 (BG7), the rover parked at the mouth of a canyon. Then it headed south, parked near a small hill between sol 3564.6 and sol 3565.6 (P7). It moved a bit and parked again between sol 3567.5 and sol 3570.5 (P8). Afterwards, the rover headed southeast between sol 3571.6 and sol 3576.6 (BG8) during which the dose rate was at a relatively stable level. Compared to BG7 and BG8, we find similar dose decreases during P7 and P8 of 9.8% and 9.9%, respectively (also see Table 1).

Figure 9c shows the OZA during P7 (shown in red) and BG7 (shown in gray). During P7, the OZA ranges from 90° towards the horizon to about 49° (most shielded in the southwest direction). During BG7, the OZA is between 90° and 62°. Figure 9d shows the ratio of blocked sky for P7 and BG7. The values integrated over θ are 32.8%, 22.1% for P7 and BG7, respectively (also shown in Table 1). Figure 9e shows the OZAduring P8 (shown in red) and BG8 (shown in gray). During P8, the OZA ranges from 90° towards the horizon to about 53° (most shielded in the west). During BG8, the OZA only ranges between 90° and 70°. Figure 9f shows the ROS for P8 and BG8. The values integrated over θ are 29.6%, 17.8% for P8 and BG8, respectively (also shown in Table 1).

4. Downward Dose and Albedo Dose

Surface particles can directly reach RAD from the non-obstructed directions, whereas downward particles from obstructed angles can not reach RAD. Based on this simple assumption, following the method of Guo et al. (2021), we can calculate the total (sum over all angles) dose rate expected for the partially obstructed sky as:

$$D_{\mathrm{GCR_H}} = \sum_{\theta=0^\circ}^{90^\circ} \mathfrak{D}_{\mathrm{GCR_H}}(\theta)\cdot\delta_\theta = \sum_{\theta=0^\circ}^{90^\circ} (1-\mathrm{ROS}(\theta))\cdot d_{\mathrm{GCR_H}}(\theta)\cdot\delta_\theta \quad (2)$$

$$D_{\mathrm{GCR_{He}}} = \sum_{\theta=0^\circ}^{90^\circ} \mathfrak{D}_{\mathrm{GCR_{He}}}(\theta)\cdot\delta_\theta = \sum_{\theta=0^\circ}^{90^\circ} (1-\mathrm{ROS}(\theta))\cdot d_{\mathrm{GCR_{He}}}(\theta)\cdot\delta_\theta \quad (3)$$

The term 1-ROS(θ) is the ratio of the unblocked sky to a full-sky view as a function of zenith angle θ (following the definition that ROS is the ratio of the obstructed sky view to the full-sky view). $d_{\mathrm{GCR_H}}(\theta)$ and $d_{\mathrm{GCR_{He}}}(\theta)$ are the modeled dose rate as a function of zenith angle θ originating from primary GCR protons and helium ions, respectively (shown in Figure 2). δ_θ is the bin width of the zenith angle used in the integration and is set as 1° throughout this study. Consequently, $\mathfrak{D}_{\mathrm{GCR_H}}$ and $\mathfrak{D}_{\mathrm{GCR_{He}}}$ are the modeled dose rate from the partially obstructed sky as a function of zenith angle θ originating from primary GCR protons and helium ions, respectively. Finally,

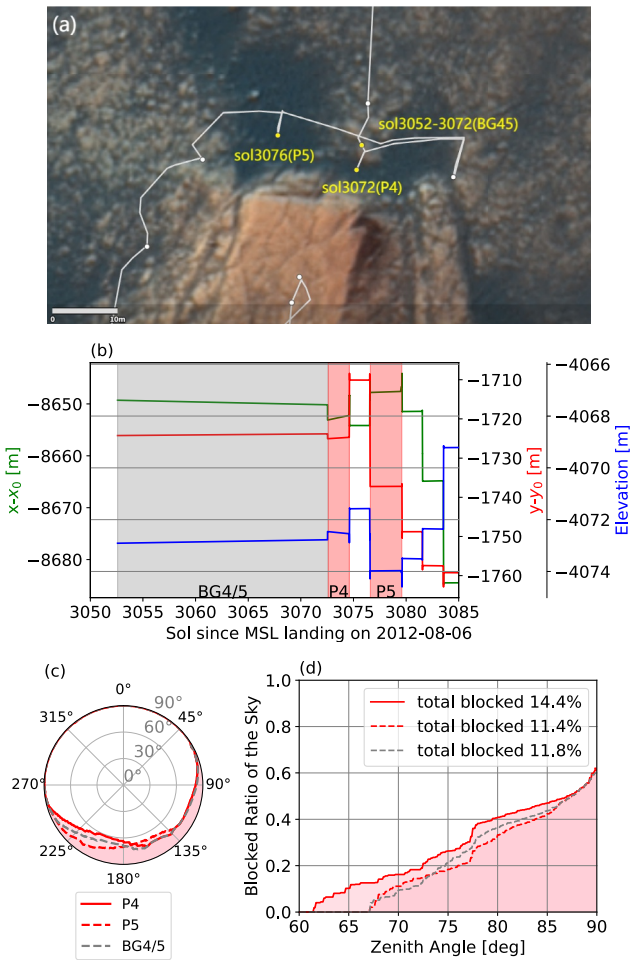

Figure 7. Similar to Figure 5, but for the Mt Mercou area.

$D_{\mathrm{GCR_H}}$ and $D_{\mathrm{GCR_{He}}}$ are the θ-integrated total dose resulting from primary GCR protons and helium ions, respectively.

Now, we consider the specific topographical scenario of Tower Buttes (Section 3.1) and the corresponding estimations of the downward dose originating from GCR protons and helium ions combining the zenith-angle model (Section 2) and the above equations. For a completely flat terrain without any surface obstruction, 1-ROS(θ) is unity since ROS(θ) is 0. Following Equation 2 and considering a full-sky (FS) view without any obstruction, we can derive $\mathfrak{D}_{\mathrm{GCR_H}}(\theta)$ under a ϕ value of 384.5 MV (modulation condition for BG1) shown as a gray curve in Figure 10a. The zenith-angle integrated dose is $D^{FS}_{\mathrm{GCR_H}} = 196.04$ μGy/d. Similarly, based on Equation 3, we derive the full-sky $\mathfrak{D}_{\mathrm{GCR_{He}}}(\theta)$ shown as a gray curve in Figure 10b and the zenith-angle integrated dose is $D^{FS}_{\mathrm{GCR_{He}}} = 36.32$ μGy/d.

For the realistic case of BG1, we use ROS(θ) for BG1 shown in Figure 5d to multiply the modeled $d_{\mathrm{GCR_H}}(\theta)$ under the modulation condition for BG1 ($\phi = 384.5$ MV) and obtain $\mathfrak{D}_{\mathrm{GCR_H}}(\theta)$ shown as a black curve in Figure 10a. The zenith-angle integrated dose rate is $D^{\mathrm{BG1}}_{\mathrm{GCR_H}} = 181.66$ μGy/d. Likewise, we derive dose $\mathfrak{D}_{\mathrm{GCR_{He}}}(\theta)$ originating from primary helium ions during BG1 shown in black in Figure 10b and the zenith-angle integrated dose rate is $D^{\mathrm{BG1}}_{\mathrm{GCR_{He}}} = 35$ μGy/d.

Similarly, given the modulation condition and specific topography of P1, we obtain $\mathfrak{D}_{\mathrm{GCR_H}}(\theta)$ and $\mathfrak{D}_{\mathrm{GCR_{He}}}(\theta)$ shown as red curves in Figures 10a and 10b, respectively. The zenith-angle integrated dose rate originating from GCR protons is $D^{\mathrm{P1}}_{\mathrm{GCR_H}} = 168.95$ μGy/d, which is about 86.1% of the full sky view dose rate, and about 92.6% of the dose rate during BG1. The zenith-angle integrated dose rate originating from GCR helium ions is $D^{\mathrm{P1}}_{\mathrm{GCR_{He}}} = 33.57$ μGy/d, which is about 92.4% of the full sky view dose rate, and about 95.7% of the dose rate during BG1.

Based on the same procedure, the dose rates during BG2 and P2 are also calculated and the results are shown in Figures 10a and 10b as dashed lines. The values of $D^{\mathrm{P2}}_{\mathrm{GCR_H}}$ and $D^{\mathrm{P2}}_{\mathrm{GCR_{He}}}$ are slightly lower than those during P1, due to slightly enhanced shielding (the total blocked sky ratio for P1 is 13.7% and for P2 is 14.8%) and slightly higher solar modulation potential.

The above calculations are applied to other locations with the results shown in Figures 10c–10j for Bloodstone Hill, Mt Mercou, Maria Gordon Notch, Paraitepuy, respectively.

Additional contributions to dose by GCR heavy ions have been quantified to be about 10% based on simulations using the atmosphere conditions at Gale Crater (Matthiä et al., 2017; Röstel et al., 2020; Zhang et al., 2022). Following Guo et al. (2021), we approximate the total dose rate D_{sky} contributed by all GCRs arriving from the sky direction as:

$$D_{\mathrm{sky}} = 1.1 \cdot (D_{\mathrm{GCR_H}} + D_{\mathrm{GCR_{He}}}) \quad (4)$$

The dose values derived from the GCR protons and helium ions and the total dose considering additional heavier ion contributions in each site (P1 to P8, BG1 to BG8) are summarized in Table 1. In most cases, the expected (from the model) downward dose rate drop (9th column) is larger than the observed decreases (4th column). For example, comparing P1 and BG1, the modeled total sky dose drop is 6.5% whereas the observed dose drop is 4%. For Maria Gordon Notch, comparing P6 and BG6, the modeled total sky dose drop is 24%, whereas the observed dose drop is 17%.

These results are expected because the shielding structure blocks the dose from the sky but meanwhile contributes to the albedo radiation so that the final reduction is less significant. However, for P5, the modeled dose decrease is

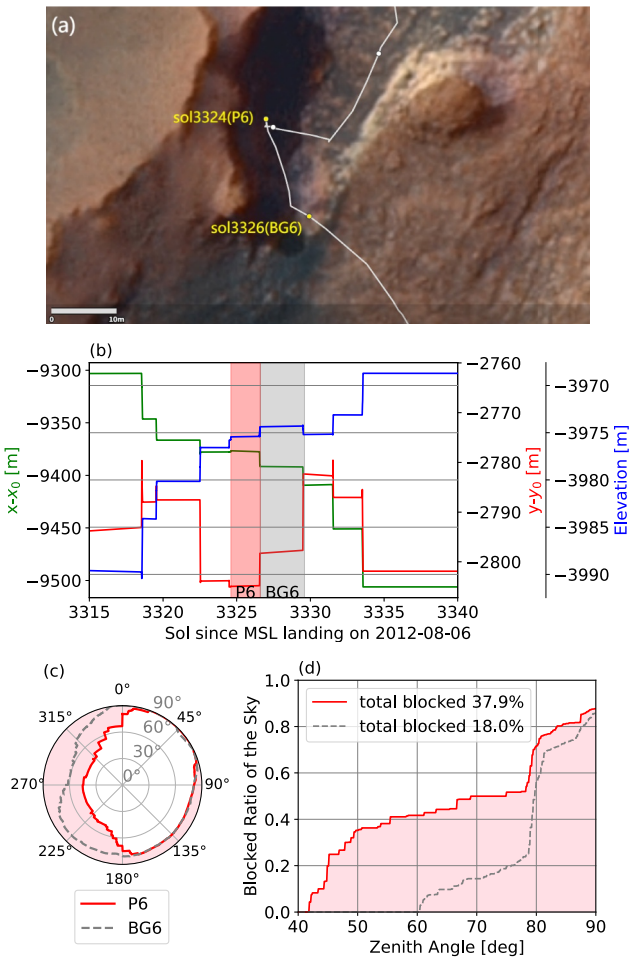

Figure 8. Similar to Figure 5, but for the Maria Gordon Notch area.

slightly smaller than the observed decrease. This might be related to the total shielding of P5 being comparable to the background period of BG4/5. The zenith-angle integrated ROS of P5 is 11.4% while that of BG4/5 is 11.8%. that is, the additional albedo dose contributed by enhanced shielding (more details on albedo radiation are given later) is even slightly higher for BG4/5. Consequently, the actual reduction is even slightly larger for P5 than the expected reduction only from downward doses.

Using the measured and modeled total dose rate, we can also derive the albedo radiation dose using the method proposed by Guo et al. (2021). We assume that the albedo radiation generated by the shielding structure is similar to that from the ground regolith, and the total albedo dose only depends on the effective geometric area of the regolith source. Defining the dose rate contributed by a completely flat terrain (FT) to be D_{albedo} (i.e., when the sky and the terrain each occupies half of the full 4π solid angle), we formulate the total dose rate on a terrain with obstruction as below:

$$\left(1+\sum_{\theta=0^\circ}^{90^\circ}\mathrm{ROS}(\theta)\cdot\delta_\theta\right)D_{\mathrm{albedo}}+D_{\mathrm{sky}}=D_{\mathrm{RAD}}, \quad (5)$$

where $\sum_{\theta=0^\circ}^{90^\circ}\mathrm{ROS}(\theta)\cdot\delta_\theta$ is the zenith-angle integrated blocked ratio of the sky that contributes additionally to the albedo radiation. Its value has been derived for each site as shown in Table 1. D_{sky} is the remaining dose of particles propagating from the atmosphere and has been derived for the above different scenarios, as shown in Table 1. D_{RAD} is the final total dose rate recorded by RAD as also listed in Table 1 for different sites. Consequently, we can calculate D_{albedo} based on the above equation with the result given in Table 1 for each terrain (P1-8 and BG1-8).

The proportion of D_{albedo} to the total surface dose (on a flat terrain) is also shown in Table 1 and has similar and consistent values within a selected area, for example, 21.5%–21.7% for Tower Buttes, 18.8%–19.4% for Mt Mercou. But for Maria Gordon Notch, D_{albedo} is derived as 55.2 μGy/d for P6, but 70.0 μGy/d for BG6. This might be due to the fact that the rover was passing a very narrow valley where the OZA was down to 42° and 37.9% of the sky was blocked during P6. Even for the "background" (BG6), 18% of the sky was still shaded. In this extreme case, the assumption that the albedo radiation generated by the obstructor has a directionality similar to that from the ground regolith is less reliable since the primary particles reaching the obstructor can also differ significantly from those on a flat ground (as will be discussed in detail in Section 5).

In general, the derived ratios of albedo dose to the total dose (on a flat terrain), that is, $D_{\mathrm{albedo}}/D_{\mathrm{RAD}}$, for different sites are in the range of 18%–24%, which is in agreement with the result of 19% estimated by Guo et al. (2021). The ratio of the last site "Paraitepuy" is larger than that of the other sites. This might be due to the much higher solar modulation condition in August 2022 in comparison to the previous sites. The relative contribution by higher-energy GCR particles in comparison to less energetic GCRs is enhanced under stronger solar modulations, and they are more efficient in producing albedo particles because of their deeper penetrating depth. Consequently, one would expect a higher albedo ratio during solar maximum than during solar minimum. However, the quantification of the dependence of the albedo ratio on the solar modulation potential still needs further investigation with more statistics.

5. Summary and Discussion

Within Gale Crater, NASA's rover Curiosity has been passing through terrains with interesting topographies, including canyons, hills, buttes, etc. These locations not only provide shielding from radiation, but also give us the unique opportunity to study their more complex influence on radiation doses detected by RAD (Ehresmann et al., 2021; Guo et al., 2021).

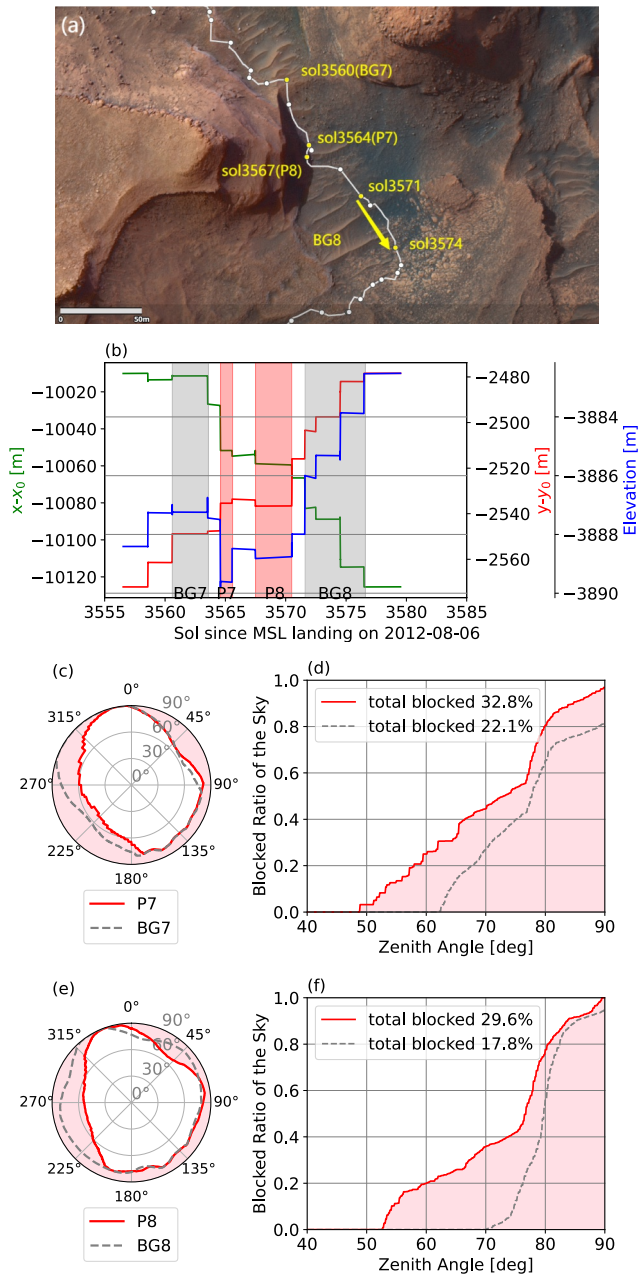

Figure 9. Similar to Figure 5, but for the Paraitepuy area.

Here we studied the rover path when Curiosity passed Tower Buttes, Bloodstone Hill, Mt Mercou, Maria Gordon Notch, and Paraitepuy. For each site, we checked the rover paths using both the rover traverse map, the rover x–y coordinates and its elevation. We then focused on some representative parking locations (named P1-P8) and background periods (BG1-BG8) for which we derived the panoramic sky visibility of RAD, and then calculated the ratio of the obstructed sky view to a full-sky view which ranges from 5.4% (BG2) to 37.9% (P6).

We also employed a Mars surface zenith-dependent dose model (Khaksari et al., 2025; Khaksarighiri et al., 2023) to derive the surface downward dose rate. As input to the model, we deduced a more accurate heliospheric modulation of GCRs at Mars, that is, the daily modulation potential ϕ, derived from the daily dose rate data measured by the TGO orbiting Mars.

Following the methodology provided by Guo et al. (2021) and using the specific panoramic sky visibility information at each site, we modeled the surface dose rate coming from the sky direction in different terrain scenarios. We found that the predicted decrease of modeled dose rate from the sky is almost always larger than the dose reduction measured by RAD. That is reasonable since the obstructing terrain on the one hand reduces the radiation from the sky while it on the other hand contributes to additional albedo radiation. Based on this idea and combining the above model and measurements, we finally derived the albedo dose on a flat terrain to be 18%–24% of the total dose, consistent with previous observational and modeling results (Guo et al., 2021; Matthiä & Berger, 2017).

Nevertheless, there are some uncertainties in the current model. First, the contribution of heavy ions to the surface dose is approximated by a fixed value of 10%. According to Zhang et al. (2022) (Figure 7), this ratio may change under different solar modulation and surface pressure conditions. In particular, when the surface pressure is lower (below ~650 Pa), the heavy ion contribution increases to ~12% at 500 Pa, while its contribution decreases to ~8% under a higher pressure of about 1,000 Pa. As a result, the final-obtained albedo dose may also have a discrepancy up to ±~ 2% when considering this pressure variation for different seasons in Gale Crater. Second, the surface albedo dose may also depend on the composition of the subsurface layers. As modeled by Röstel et al. (2020), the absorbed dose can be slightly smaller when the surface material is more hydrated (i.e., more hydrogen). When the composition of the obstructor is highly different from the surrounding terrain, the previous assumption (that the albedo radiation generated by the obstructing structure is similar to that from the ground regolith) is less accurate. Third, the approximation that albedo radiation is isotropic is based on previous Martian radiation simulations considering a flat surface (Appel et al., 2018). However, this may be inaccurate, in particular at sites where the obstructor is highly oblique and self-shielded (e.g., Maria Gordon Notch, Figure 8). In such cases, primary particles reaching the obstructor can be much less than those for a less-shielded terrain and their energy/angular distribution may also be different from that on a flat surface, so that the secondaries generated from the obstructor reaching RAD cannot be considered as similar to those from the ground. There do exist methodologies to consider a more accurate terrain effect in post treatment of the simulated flux, which, however, also have other uncertainties (Charpentier et al., 2026). Last but not least, the current study relies on the calculated cutoff elevation angle of the horizon within a radius of 20 km around the observation point. A larger radius will include more far-way structures which may potentially have a shielding effect on the surface dose, but will bear more atmospheric effects on albedo particles. Specifically, the atmosphere between a terrain obstruction and the rover will in theory also modify the albedo particles generated by the obstructor and this effect becomes stronger when the obstructor is further away. Unfortunately, it is non-trivial to consider this effect with the current model setup. Accurate particle transport modeling including the

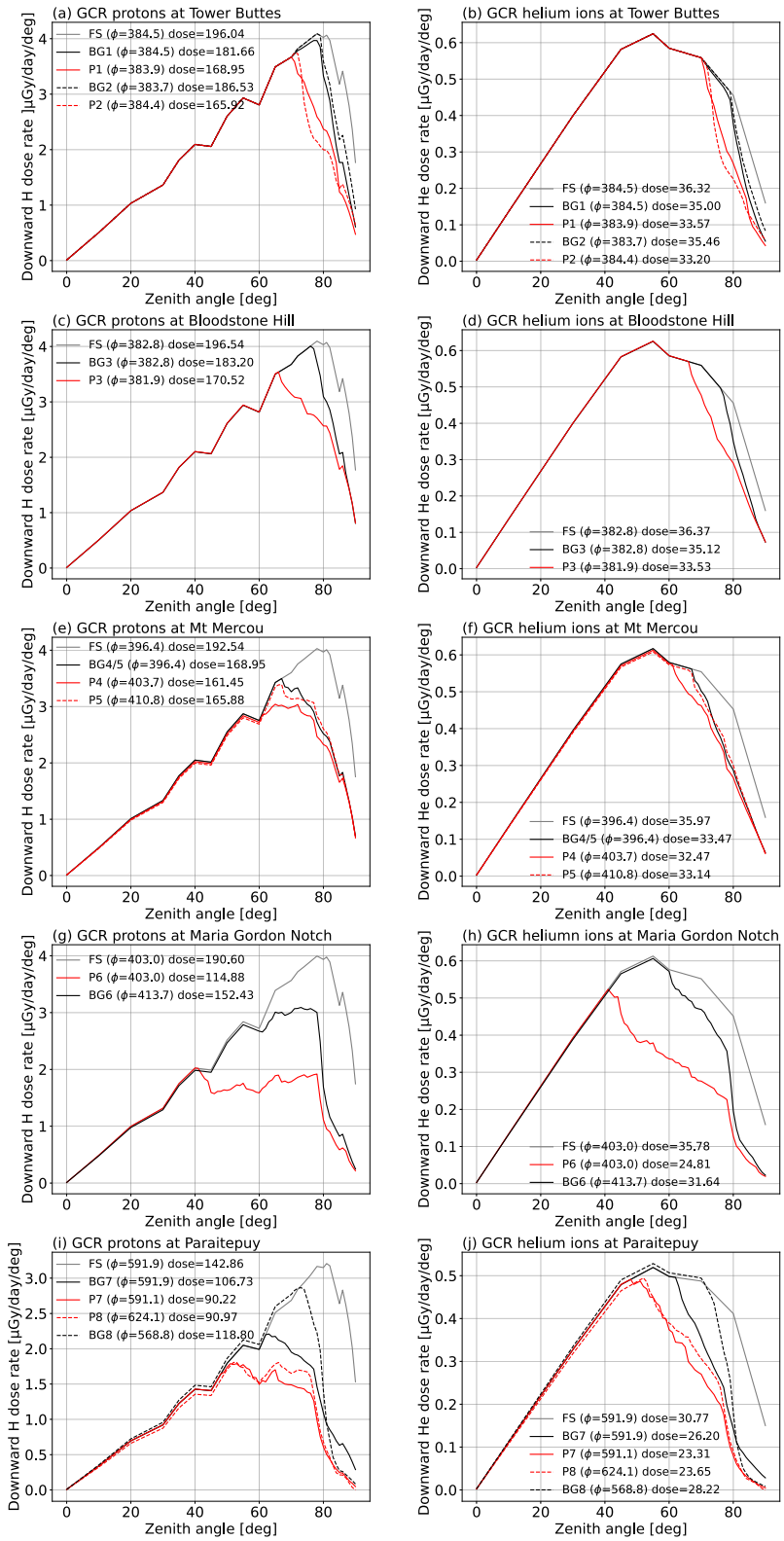

Figure 10. The dose rate resulting from particles arriving from the sky as a function of zenith angle θ for primary GCR protons (left) and helium ions (right) under different terrain scenarios (shown in different rows). In each case, the dose rate (μGy/d) integrated over θ is marked in the legend, where FS stands for full sky without any obstruction, BG# or P# represent each background or parking period. The average modulation potential in each period is also noted within the brackets of the legend.

complex and realistic surface geometry in the radiation model would be a better approach, but it is going to be computationally expensive.

Moreover, we note that the dose values considered in this work refer to the "absorbed dose in the tissue-like plastic detector" which is the total energy deposited by all particles reaching detector "E" divided by its mass (in J/kg or Gray). This should not be confused with the body effective dose (in Sv), which is widely used in various radiation protection regulations and reflects the health risk of radiation to the entire human body (ICRP, 2007). Considering radiation damage to biological tissues, one can take into account the ionization density along the particle track, characterized by LET (often in units of keV/μm); then for each particle track, one can multiply the absorbed dose with the LET-dependent quality factor Q(LET), thus calculating the dose equivalent. Dose equivalent can be obtained by either radiation models or dosimetry measurements. When assessing radiation damage to an entire organism, one should sum the organ-weighted dose equivalent values in different critical organs to obtain the total-body effective dose (also in Sv), which is normally only quantified by radiation models and very difficult to measure directly. Since the RAD LET viewing cone is only up to 36° from the vertical axis of the detector (Hassler et al., 2012), it remains unshielded even when the rover is close to a butte. Thus, the LET measurement spectra would not be affected by the surface-structural shielding, nor would the measurement-derived average quality factor $<Q>$ change. Therefore, the surface dose equivalent under a shielded scenario cannot be accurately assessed from RAD measurements alone. Future studies based on particle radiation transport modeling including complex and realistic Mars surface geometry will be essential to evaluate the shielding effect on effective dose, which is a critical factor for future crewed Mars surface missions.

In conclusion, our study adopted 8 new sites along the rover path and found that the decrease in the dose rate due to surface shielding can reach 19%. Based on these observations and a zenith-dependent radiation model, we also estimate that the Martian surface albedo dose is between 18% and 24% of the total absorbed dose. This study contributes to developing a realistic terrain-based radiation map that is important for future Mars explorers.

Conflict of Interest

The authors declare no conflicts of interest relevant to this study.

Availability Statement

MSL data are archived within the NASA planetary data system (Peterson et al., 2013). The zenith-dependent Mars surface radiation model is available at Guo (2021).

Acknowledgments
JG, CT, and LP acknowledge the support by the National Natural Science Foundation of China (Grants 42521007, 42130204, 42188101, 42474221) and the National Key R&D Program of China (2025YFF0510900). RAD is supported by NASA (HEOMD) under Jet Propulsion Laboratory (JPL) subcontract 1273039 to Southwest Research Institute and in Germany by the German Aerospace Center (DLR) and DLR's Space Administration Grant 50QM1701 to the Christian Albrechts-Universität zu Kiel. GC's work, bearing the reference EUR CARe N°ANR-18-EURE-0003, has benefited from support managed by the Agence Nationale de la Recherche under the Programme Investissements d'Avenir.

References

Agostinelli, S., Allison, J., Amako, K., Apostolakis, J., Araujo, H., Arce, P., et al. (2003). GEANT4: A simulation toolkit. *Nuclear Instruments & Methods in Physics Research, Section A*, *506*(3), 250–303. https://doi.org/10.1016/S0168-9002(03)01368-8

Allison, J., Amako, K., Apostolakis, J., Araujo, H., Arce Dubois, P., Asai, M., et al. (2006). Geant4 developments and applications. *IEEE Transactions on Nuclear Science*, *53*(1), 270–278. https://doi.org/10.1109/TNS.2006.869826

Allison, J., Amako, K., Apostolakis, J., Arce, P., Asai, M., Aso, T., et al. (2016). Recent developments in Geant4. *Nuclear Instruments and Methods in Physics Research Section A: Accelerators, Spectrometers, Detectors and Associated Equipment*, *835*, 186–225. https://doi.org/10.1016/j.nima.2016.06.125

Appel, J. K., Köhler, J., Guo, J., Ehresmann, B., Zeitlin, C., Matthiä, D., et al. (2018). Detecting upward directed charged particle fluxes in the Mars science laboratory radiation assessment detector. *Earth and Space Science*, *5*(1), 2–18. https://doi.org/10.1002/2016EA000240

Charpentier, G., Ehresmann, B., Guo, J., Khaksarighiri, S., Bénacquista, R., Malapert, J. C., et al. (2026). Influence of Mars topography on neutral surface radiation: Modeling and MSL/RAD observations. *Journal of Geophysical Research: Planets*, *131*, e2025JE009336. https://doi.org/10.1029/2025JE009336

Charpentier, G., Ruffenach, M., Benacquista, R., Ecoffet, R., Cappe, A., Dossat, C., et al. (2024). ARAMIS: A Martian radiative environment model built from GEANT4 simulations. *Journal of Space Weather and Space Climate*, *14*, 35. https://doi.org/10.1051/swsc/2024032

Cucinotta, F. A., To, K., & Cacao, E. (2017). Predictions of space radiation fatality risk for exploration missions. *Life Sciences and Space Research*, *13*, 1–11. https://doi.org/10.1016/j.lssr.2017.01.005

De Angelis, G., Wilson, J., Clowdsley, M., Qualls, G., & Singleterry, R. (2006). Modeling of the Martian environment for radiation analysis. *Radiation Measurements*, *41*(9), 1097–1102. https://doi.org/10.1016/j.radmeas.2006.04.032

Dibb, S. D., Hardgrove, C., Lightholder, J., Heffern, L., & Ehresmann, B. (2024). Observed correlation between local topography and passive neutron measurements from the dynamic albedo of neutrons (DAN) instrument on the Mars science laboratory (MSL) rover. *Earth and Space Science*, *11*(10), e2023EA003130. https://doi.org/10.1029/2023EA003130

Ehresmann, B., Hassler, D., Zeitlin, C., Guo, J., Wimmer-Schweingruber, R., Khaksari, S., et al. (2021). Natural radiation shielding on Mars measured with the MSL/RAD instrument. *Journal of Geophysical Research: Planets*, *126*(8), e2021JE006851. https://doi.org/10.1029/2021JE006851

Freiherr von Forstner, J. L., Guo, J., Wimmer-Schweingruber, R. F., Dumbović, M., Janvier, M., Démoulin, P., & Zeitlin, C. J. (2020). Comparing the properties of ICME-induced forbush decreases at Earth and. *MARS*, *125*(3), e27662. https://doi.org/10.1029/2019JA027662

Gómez-Elvira, J., Armiens, C., Castañer, L., Domínguez, M., Genzer, M., Gómez, F., et al. (2012). REMS: The environmental sensor suite for the Mars science laboratory rover. *Space Science Reviews*, *170*(1–4), 583–640. https://doi.org/10.1002/2013JE004525

Gronoff, G., Norman, R. B., & Mertens, C. J. (2015). Computation of cosmic ray ionization and dose at Mars. I: A comparison of HZETRN and planetocosmics for proton and alpha particles. *Advances in Space Research*, *55*(7), 1799–1805. https://doi.org/10.1016/j.asr.2015.01.028

Grotzinger, J. P., Crisp, J., Vasavada, A. R., Anderson, R. C., Baker, C. J., Barry, R., et al. (2012). Mars science laboratory mission and science investigation. *Space Science Reviews*, *170*(1), 5–56. https://doi.org/10.1007/s11214-012-9892-2

Guo, J. (2021). Directionality of the Martian surface radiation and derivation of the upward albedo radiation [Dataset]. *Zenodo*. https://doi.org/10.5281/zenodo.4701689

Guo, J., Banjac, S., Röstel, L., Terasa, J. C., Herbst, K., Heber, B., & Wimmer-Schweingruber, R. F. (2019). Implementation and validation of the GEANT4/AtRIS code to model the radiation environment at Mars. *Journal of Space Weather and Space Climate*, *9*(A2). https://doi.org/10.1051/swsc/2019004

Guo, J., Khaksarighiri, S., Wimmer-Schweingruber, R. F., Hassler, D. M., Ehresmann, B., Zeitlin, C., et al. (2021). Directionality of the Martian surface radiation and derivation of the upward albedo radiation. *Geophysical Research Letters*, *48*(15), e2021GL093912. https://doi.org/10.1029/2021GL093912

Guo, J., Zeitlin, C., Wimmer-Schweingruber, R. F., Rafkin, S., Hassler, D. M., Posner, A., et al. (2015). Modeling the variations of dose rate measured by RAD during the first MSL Martian year: 2012–2014. *The Astrophysical Journal*, *810*(1), 24. https://doi.org/10.1088/0004-637X/810/1/24

Hassler, D. M., Zeitlin, C., Wimmer-Schweingruber, R. F., Böttcher, S. I., Martin, C., Andrews, J., et al. (2012). The radiation assessment detector (RAD) investigation. *Space Science Reviews*, *170*(1), 503–558. https://doi.org/10.1007/s11214-012-9913-1

Honig, T., Witasse, O. G., Evans, H., Nieminen, P., Kuulkers, E., Taylor, M. G., et al. (2019). Multi-point galactic cosmic ray measurements between 1 and 4.5 au over a full solar cycle. *Annales Geophysicae*, *37*(5), 903–918. https://doi.org/10.5194/angeo-37-903-2019

ICRP. (2007). ICRP publication 103: The 2007 recommendations of the international commission on radiological protection. *Annals of the ICRP*, *37*(2), 1–332. https://doi.org/10.1016/j.icrp.2007.10.003

Keating, A., Mohammadzadeh, A., Nieminen, P., Maia, D., Coutinho, S., Evans, H., et al. (2005). A model for Mars radiation environment characterization. *IEEE Transactions on Nuclear Science*, *52*(6), 2287–2293. https://doi.org/10.1109/TNS.2005.860748

Khaksari, S., Phipps, P. H., Wimmer-Schweingruber, R. F., Stubbs, T. J., Looper, M. D., Guo, J., et al. (2025). Radiation transport through the Martian atmosphere as a function of the zenith angle. *Journal of Geophysical Research: Planets*, *130*(12), e2025JE009352. https://doi.org/10.1029/2025JE009352

Khaksarighiri, S., Guo, J., Wimmer-Schweingruber, R. F., Löffler, S., Ehresmann, B., Matthiä, D., et al. (2023). The zenith-angle dependence of the downward radiation dose rate on the Martian surface: Modeling versus MSL/RAD measurement [Article]. *Journal of Geophysical Research: Planets*, *128*(4), e2022JE007644. (All Open Access, Green Open Access, Hybrid Gold Open Access). https://doi.org/10.1029/2022JE007644

Kim, M.-H. Y., Cucinotta, F. A., Nounu, H. N., Zeitlin, C., Hassler, D. M., Rafkin, S. C. R., et al. (2014). Comparison of Martian surface ionizing radiation measurements from MSL-RAD with Badhwar-O'Neill 2011/HZETRN model calculations. *Journal of Geophysical Research: Planets*, *119*(6), 1311–1321. https://doi.org/10.1002/2013JE004549

Lee, C., Hara, T., Halekas, J., Thiemann, E., Chamberlin, P., Eparvier, F., et al. (2017). Maven observations of the solar cycle 24 space weather conditions at Mars. *Journal of Geophysical Research: Space Physics*, *122*(3), 2768–2794. https://doi.org/10.1002/2016JA023495

Litvak, M., Mitrofanov, I., Barmakov, Y., Behar, A., Bitulev, A., Bobrovnitsky, Y., et al. (2008). The dynamic albedo of neutrons (DAN) experiment for NASA'S 2009 Mars science laboratory. *Astrobiology*, *8*(3), 605–612. (PMID: 18598140). https://doi.org/10.1089/ast.2007.0157

Liu, W., Guo, J., Wang, Y., & Slaba, T. C. (2024). A comprehensive comparison of various galactic cosmic-ray models to the state-of-the-art particle and radiation measurements. *The Astrophysical Journal Supplement Series*, *271*(1), 18–47. https://doi.org/10.3847/1538-4365/ad18ad

Liu, W., Guo, J., Zhang, J., & Semkova, J. (2023). Modeling the radiation environment of energetic particles at Mars orbit and a first validation against TGO measurements. *The Astrophysical Journal*, *949*(2), 77. https://doi.org/10.3847/1538-4357/acce3c

Matthiä, D., & Berger, T. (2017). The radiation environment on the surface of Mars–numerical calculations of the galactic component with GEANT4/planetocosmics. *Life Sciences and Space Research*, *14*, 57–63. https://doi.org/10.1016/j.lssr.2017.03.005

Matthiä, D., Ehresmann, B., Lohf, H., Köhler, J., Zeitlin, C., Appel, J., et al. (2016). The Martian surface radiation Environment–A comparison of models and MSL/RAD measurements. *Journal of Space Weather and Space Climate*, *6*(27), 1–17. https://doi.org/10.1051/swsc/2016008

Matthiä, D., Hassler, D. M., de Wet, W., Ehresmann, B., Firan, A., Flores-McLaughlin, J., et al. (2017). The radiation environment on the surface of Mars—Summary of model calculations and comparison to RAD data. *Life Sciences and Space Research*, *14*, 18–28. https://doi.org/10.1016/j.lssr.2017.06.003

O'Neill, P. M., Golge, S., & Slaba, T. C. (2015). *Badhwar-O'Neill 2014 galactic cosmic ray flux model description*. (Tech. Rep. No. NASA/TP-2015-218569). Johnson Space Center, National Aeronautics and Space Administration (NASA). Retrieved from http://www.sti.nasa.gov

Peterson, J., Rafkin, S., Zeitlin, C., Ehresmann, B., Weigle, E., Jeffers, S., & Hassler, D. M. O. (2013). MSL Mars radiation assessment detector RDR V1.0, MSL-M-RAD-3-RDR-V1.0. (NASA Planetary Data System). https://doi.org/10.17189/1519761

Potgieter, M. S. (2013). Solar modulation of cosmic rays [Article]. *Living Reviews in Solar Physics*, *10*. (All Open Access, Gold Open Access). https://doi.org/10.12942/lrsp-2013-3

Rafkin, S. C., Zeitlin, C., Ehresmann, B., Hassler, D., Guo, J., Köhler, J., et al. (2014). Diurnal variations of energetic particle radiation at the surface of Mars as observed by the Mars science laboratory radiation assessment detector. *Journal of Geophysical Research: Planets*, *119*(6), 1345–1358. https://doi.org/10.1002/2013JE004525

Röstel, L., Guo, J., Banjac, S., Wimmer-Schweingruber, R. F., & Heber, B. (2020). Subsurface radiation environment of Mars and its implication for shielding protection of future habitats. *Journal of Geophysical Research: Planets*, *125*(3), e2019JE006246. https://doi.org/10.1029/2019JE006246

Roussos, E., Dialynas, K., Krupp, N., Kollmann, P., Paranicas, C., Roelof, E. C., et al. (2020). Long- and short-term variability of galactic cosmic-ray radial intensity gradients between 1 and 9.5 au: Observations by Cassini, BESS, BESS-polar, PAMELA, and AMS-02. *The Astrophysical Journal*, *904*(2), 165. https://doi.org/10.3847/1538-4357/abc346

Saganti, P. B., Cucinotta, F. A., Wilson, J. W., Simonsen, L. C., & Zeitlin, C. (2004). Radiation climate map for analyzing risks to astronauts on the Mars surface from galactic cosmic rays. *Space Science Reviews*, *110*(1–2), 143–156. https://doi.org/10.1007/978-0-306-48600-5_5

Semkova, J., Koleva, R., Benghin, V., Dachev, T., Matviichuk, Y., Tomov, B., et al. (2018). Charged particles radiation measurements with Liulin-MO dosimeter of FREND instrument aboard ExoMars trace gas orbiter during the transit and in high elliptic Mars orbit. *Icarus*, *303*, 53–66. https://doi.org/10.1016/j.icarus.2017.12.034

Usoskin, I., Bazilevskaya, G., & Kovaltsov, G. (2011). Solar modulation parameter for cosmic rays since 1936 reconstructed from ground-based neutron monitors and ionization chambers. *Journal of Geophysical Research*, *116*(A2), A02104. https://doi.org/10.1029/2010JA016105

Walsh, L., Schneider, U., Fogtman, A., Kausch, C., McKenna-Lawlor, S., Narici, L., et al. (2019). Research plans in Europe for radiation health hazard assessment in exploratory space missions. *Life Sciences and Space Research*, *21*, 73–82. https://doi.org/10.1016/J.LSSR.2019.04.002

Wimmer-Schweingruber, R. F., Köhler, J., Hassler, D. M., Guo, J., Appel, J.-K., Zeitlin, C., et al. (2015). On determining the zenith angle dependence of the Martian radiation environment at gale crater altitudes. *Geophysical Research Letters*, *42*(24), 10557–10564. https://doi.org/10.1002/2015gl066664

Zeitlin, C., Hassler, D., Wimmer-Schweingruber, R. F., Ehresmann, B., Appel, J., Berger, T., et al. (2016). Calibration and characterization of the radiation assessment detector (RAD) on curiosity. *Space Science Reviews*, *201*(1–4), 201–233. https://doi.org/10.1007/s11214-016-0303-y

Zhang, J., Guo, J., Dobynde, M. I., Wang, Y., & Wimmer-Schweingruber, R. F. (2022). From the top of Martian Olympus to deep craters and beneath: Mars radiation environment under different atmospheric and regolith depths. *Journal of Geophysical Research: Planets*, *127*(3), e2021JE007157. https://doi.org/10.1029/2021JE007157